# 

NASA TECHNICAL MEMORANDUM USA USPACE ON SPACE OF THE PROPERTY OF THE PRO

NASA TM X-854

X 63 16648

Corles 2

NASA TM X-854

 $32\rho$ 

UNCLASSIFIED

10 7047 8-27-70

APOLLO FOREBODY PRESSURE
AND HEAT-TRANSFER DISTRIBUTIONS

IN HELIUM AT  $M_{\infty} = 20$ 

Declassified by authority of NASA Classification Change Notices No. (Dated \*\*/

by Joseph G. Marvin, Thorval Tendeland, and Marvin Kussoy

Ames Research Center

Moffett Field, California



NATIONAL AERONAUTICS AND SPACE ADMINISTRATION • WASHINGTON, D. C. • NOVEMBER 1963





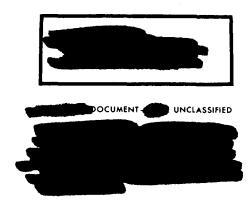
# TECHNICAL MEMORANDUM X-854

# APOLLO FOREBODY PRESSURE AND HEAT-TRANSFER

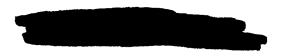
DISTRIBUTIONS IN HELIUM AT  $M_{\infty} = 20$ 

By Joseph G. Marvin, Thorval Tendeland, and Marvin Kussoy Washington, NASA, Nov. 1963

Moffett Field, Calif.



NATIONAL AERONAUTICS AND SPACE ADMINISTRATION



# NATIONAL AERONAUTICS AND SPACE ADMINISTRATION

TECHNICAL MEMORANDUM X-854

APOLLO FOREBODY PRESSURE AND HEAT-TRANSFER

DISTRIBUTIONS IN HELIUM AT  $M_{\infty} = 20$ \*

By Joseph G. Marvin, Thorval Tendeland, and Marvin Kussoy

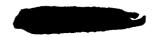
#### SUMMARY

Tests were performed over an angle-of-attack range from 0° to 33° and at a Reynolds number based on maximum body diameter of 1.85×10°. The flow over the forebody changed from axisymmetric to nonaxisymmetric with increasing angle of attack, but the normalized heat-transfer distribution along the vertical plane of symmetry was predicted adequately from measured pressure distributions by axisymmetric theory. The maximum heat transfer at angle of attack did not occur at the stagnation point but on the small corner radius of the windward surface.

A study of the pressure and heating-rate distributions on the forebody suggested that enthalpy level does not change the heating-rate distribution significantly. A comparison of air and helium data tended to verify this conclusion.

#### INTRODUCTION

An important part of the project Apollo capsule is the heat shield for reentry into the earth's atmosphere. To provide adequate thermal protection with a minimum of weight it is necessary to know the heating rates with reasonable accuracy. Therefore the parameters which affect the heating rates, such as pressure distribution, velocity gradients, Mach number, etc., have been investigated in a number of test facilities. The purpose of the present report is: (1) to describe measurements obtained in helium at  $M_{\infty}$  = 20; (2) to correlate pressure distributions, velocity gradients, and heating rates and to compare these data with existing theories; (3) to evaluate the effects of differences in gas composition and properties upon the heating rates and heating-rate predictions.





$c_p$	specific heat at constant pressure
h	coefficient of heat transfer, $\frac{q}{T_r - T_W}$
$\frac{h}{h_0,\alpha=0^0}$	ratio of local heat-transfer coefficient to the stagnation-point heat-transfer coefficient at zero angle of attack
Н	fluid enthalpy, $c_pT$
L	axial distance along the nozzle center line measured from the begin- ning of the test section and in the direction of the free stream
7	normal distance from the nozzle center line
${\rm M}_{\infty}$	free-stream Mach number
p	pressure
$\frac{p}{p_{t_2}}$	ratio of local surface pressure to impact pressure at the free-stream Mach number
q	heat-transfer rate normal to the body surface per unit area
R	one-half the maximum body diameter
$r_b$	spherical forebody radius
r	normal distance from a line passing through the stagnation point and in the direction of the free stream to a point on the body surface
$\mathrm{Re}_{\infty}/\mathrm{inch}$	free-stream Reynolds number per inch, $\frac{\rho_{\infty}u_{\infty}}{\mu_{\infty}}$
S	distance along the body surface measured from the stagnation point with the body at zero angle of attack
T	temperature
$u_{\infty}$	free-stream velocity
u	local velocity in s direction
w	local velocity along $\varphi' = 90^{\circ}$ meridian
S	distance along the body surface in $\phi=0^{O}$ direction measured from the true stagnation point with the body at angle of attack
X,Y	coordinates defined in figure 1





distance along body surface in the  $\phi' = 90^{\circ}$  direction measured from the true stagnation point with the body at angle of attack

angle of attack measured from the axis of symmetry and the free-stream vector

isentropic exponent

 $\mathbf{z}$ 

 $\gamma_{\bullet}$ 

r

fluid density

azimuth angle as defined in figure l

azimuth angle as defined in figure 8

 $\theta_{\mathbf{w}}$ ' normalized enthalpy gradient at the wall

power in viscosity power law

# Subscripts

o stagnation point value

evaluated at recovery temperature

t total conditions (i.e., conditions that would exist if the gas were brought to rest isentropically)

w evaluated at the wall

conditions behind a normal shock wave

# APPARATUS

#### Models

The model configuration is shown in figure 1. For the pressure tests, the model was brass with a removable front face which was rotated so that data could be obtained at the various meridian plane angles ( $\phi$ ). The size of the model limited the number of pressure orifices that could be used during a single run. For the transient heat-transfer tests, the model was 1/32-inch-thick stainless steel (SS347) with thermocouples spot welded to the inner surface.





All tests were conducted at  $M_{\infty}=20$  and  $Re_{\infty}/inch=0.744\times10^6$  in the Ames hypersonic helium tunnel described in reference 1. Figure 2 presents the results of a Mach number survey of the  $M_{\infty}=20$  nozzle at several locations in the test section. The location of the test model varied between L=12 and 21 as the model angle of attack varied from  $0^{\circ}$  to  $33^{\circ}$ .

#### Instrumentation

All data were recorded on magnetic tape by a Beckman Model 210 high-speed recording system.

Pressures were measured with bonded strain-gage pressure transducers with a range from 0 to 10 psia. These transducers were subject to possible errors of  $\pm 0.50$  percent of full-scale reading.

Temperatures were measured with chromel-constantan thermocouples spot welded to the inner surface of the thin-shelled heat-transfer model. Temperatures were recorded every 0.10 second with  $\pm 1^{\circ}$  F precision.

#### TEST METHOD

#### Flow Visualization

Shock-wave shapes were measured from shadowgraphs of the model taken over the range of angles of attack during the pressure tests. To obtain streamline patterns over the spherical face, the forebody was coated with a mixture of vacuum pump oil, oleic acid, and  $T_iO_2$ . The model was then tested at the desired angle of attack and the streamline patterns were photographed after the tunnel was shut down. To protect the flow patterns during tunnel shutdown, a flow starting spike (see ref. l for details) was placed ahead of the model.

# Pressure Tests

The pressure transducers were calibrated before each test run. The tunnel was started with the model at  $\alpha=0^{\circ}$ . After supersonic flow was established, the model was positioned to the desired angle of attack and kept there until a constant pressure was recorded. At that time the test run was terminated.

All the pressure data were reduced to the ratio  $p/p_{t_2}$ . At some angle-of-attack positions a curve faired through the data did not pass through a value of  $p/p_{t_2}=1$ . The variation of this ratio from unity was on the order of 2 percent or less and was believed to be due to small changes in the measured  $p_{t_2}$  for





different test runs. Therefore, the value of  $p_{t_2}$  was adjusted so that a best-fit curve to the data would pass through  $p/p_{t_2}=1$  at the estimated stagnation point.

#### Heat-Transfer Tests

Heat-transfer data were obtained by the transient temperature technique described in reference 2. Errors due to neglecting skin conduction were estimated and found to be negligible except at the model corners where accurate estimates of conduction could not be obtained. Therefore all the data are presented without conduction corrections. The heat-transfer coefficient was obtained from experimental data by use of the following equation taken from reference 2:

$$\frac{q_{w}}{T_{t}p_{t}^{1/2}} = \frac{h}{p_{t}^{1/2}} \left(\frac{T_{r}}{T_{t}} - \frac{T_{w}}{T_{t}}\right) \tag{1}$$

Heating-rate data obtained at initial wall temperatures of  $-200^{\circ}$  F,  $-100^{\circ}$  F, and  $150^{\circ}$  F were plotted in the form given by equation (1). The heat-transfer coefficient and recovery temperature were obtained from such plots (see ref. 2). The estimated accuracy in obtaining heat-transfer coefficients, by this technique, was  $\pm 10$  percent.

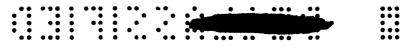
# RESULTS AND DISCUSSION

#### Flow Visualization

Shadowgraph pictures which show the shock waves over the model at angles of attack are presented in figure 3. In the vicinity of the stagnation point, the shock wave becomes more curved and moves closer to the body with increasing angle of attack. The measured shock waves are presented in figure 4. Also shown in figure 4 is a predicted shock-wave shape between the sonic points on the body as obtained from reference 3 for  $\alpha = 0^{\circ}$  to  $25^{\circ}$  (the range of applicability for this particular configuration). Agreement between predicted and measured shock-wave shapes is quite good.

To determine qualitatively the type of flow over the forebody at angle of attack, the streamline patterns were photographed over a range of angles of attack as in figure 5. The origin of the streamlines is believed to indicate the location of the stagnation region and this belief will be verified later in the report. Thus the stagnation point moves from the center of the forebody toward the windward corner with increasing angle of attack. The flow appears to depart from axisymmetric with increasing angle of attack since the stagnation point grows into a stagnation line or region resembling two-dimensional flow. Pressure distribution tests at  $\alpha = 33^{\circ}$  also indicate that in the stagnation region the flow is nonsymmetrical. This will be discussed in the following section.





# Pressure Distribution

The measured and calculated pressure distributions over the forebody will be presented and the associated variations in stagnation-point location and stagnation-point velocity gradient will be described.

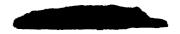
Figure 6 presents the ratio p/p<sub>t</sub> versus S/R on the Apollo forebody for several values of  $\phi$  over a range of angles of attack. Also shown are predictions for  $\phi=0^{\rm O}$  obtained from Newtonian theory and from the theory of reference 3. At  $\alpha=0^{\rm O}$  the theory of reference 3 gives a good estimate of the pressure distribution and predicts approximately the pressure decrease near the forebody corner, which Newtonian theory does not do. For the other angles of attack up to 25° the two theories bracket the measured pressures for the negative values of S/R and for the positive values of S/R less than the respective stagnation-point values. Generally, the theory of reference 3 does better in predicting the behavior of the pressure in the vicinity of the stagnation point, and Newtonian theory does somewhat better in predicting the pressures for S/R < 0. At  $\alpha=33^{\rm O}$  only the Newtonian prediction is shown and it predicts reasonably well the pressures for S/R < 0.3.

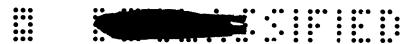
Several interesting results are derived from the pressure distribution data. Figure 7 presents the stagnation-point location (S/R) $_{0}$  versus  $\alpha$  obtained both from the pressure distributions and from the flow visualization photographs. Also shown are the predicted stagnation-point locations from the theory of reference 3 and Newtonian theory. The data and theory of reference 3 are in good agreement up to  $\alpha$  = 25 $^{0}$ , the limit of applicability of that theory, whereas Newtonian theory predicts a more rapid movement of the stagnation-point location.

Figure 8 presents the stagnation-point velocity gradient along the  $\phi=0^{O}$  meridian normalized by the Newtonian velocity gradient at  $\alpha=0^{O}$  for various angles of attack. At  $\alpha=0^{O}$  the velocity gradient is 1.31 times the Newtonian value and increases to 3.51 times Newtonian at  $\alpha=33^{O}$ . Some additional pressure data were obtained at  $\alpha=33^{O}$  along a line passing through the stagnation point in a direction  $90^{O}$  from the  $\phi=0^{O}$  meridian. The velocity gradient in this direction  $(\phi^{\bullet}=90^{O})$  is also shown in figure 8. It is readily apparent from this nonsymmetry of the velocity gradients at the stagnation point that the flow is neither axisymmetric nor two-dimensional.

# Heat Transfer

The distribution of heat-transfer coefficient  $h/h_0$ ,  $\alpha=0$  with position on the forebody, S/R, is presented in figure 9 over a range of angles of attack. Generally, these data follow the same trends as the pressure distribution data, but an interesting difference at angle of attack is that the maximum heat transfer does not occur at the stagnation point estimated from pressure measurements but at a position nearer the forebody corner. This is a result of the large pressure gradients near the corner.





To predict the heat-transfer coefficient distribution, the axisymmetric theory of Lees (ref. 4) as modified by reference 5 was used along the  $\phi=0^{O}$  meridian. The modified equation taken from reference 5 for an isothermal wall with  $M_{\infty}>\!\!>$  1 was

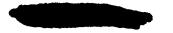
$$\frac{h}{h_{0,\alpha=0^{\circ}}} = \frac{0.5 \left(\frac{p}{p_{t_{2}}}\right) \sqrt{1 - \left(\frac{p}{p_{t_{2}}}\right)^{\frac{\gamma-1}{\gamma}}} r}}{\left[\int_{0}^{s} \left(\frac{p}{p_{t_{2}}}\right)^{\frac{\omega\gamma + (1-w)}{\gamma}} \sqrt{1 - \left(\frac{p}{p_{t_{2}}}\right)^{\frac{\gamma-1}{\gamma}}} r^{2} ds}\right]^{1/2} \sqrt{\frac{1}{u_{\infty}} \left(\frac{du}{ds}\right)_{s=0,\alpha=0^{\circ}}}$$
(2)

Equation (2) is identical to the equation for the cold wall heating-rate distribution, provided  $T_{\rm r}/T_{\rm t}=1$ ,  $\omega=1$ , and  $\gamma=\overline{\gamma}$  (an average value behind the shock wave). These are reasonable values for high Mach number equilibrium flow over blunt bodies (see ref. 4). Hence, the data presented as  $h/h_{0,\alpha=0}$ 0 can be considered equivalent to  $q/q_{0,\alpha=0}$ 0 for a cold wall. At  $\alpha=0^{\circ}$ , good agreement is obtained between the calculated values for  $h/h_{0,\alpha=0}$ 0 and the data in figure 9(a). The measured and predicted stagnation-point heat-transfer coefficients (ref. 4) agreed within 5 percent. It is interesting to compare predictions using equation (2) which is for axisymmetric flow with the data for angles of attack where the flow is no longer axisymmetric. Values along the  $\phi=0^{\circ}$  meridian predicted by equation (2) fit the data trends quite well (fig. 9) because the heat transfer over the forebody is primarily a function of local pressure conditions. Equation (2) also predicts the heating rates near the corner to be higher than the stagnation-point value. This increased heat transfer is due to a thinner boundary layer resulting from an increase in local velocity gradient. The method of Kemp, Rose, and Detra (ref. 6) was also used to estimate the effects of velocity gradient on equation (2). The correlation given in reference 6 can be used to write the ratio of heat-transfer coefficients or cold-wall heating-rate ratio as,

$$\frac{h}{h_{0,\alpha=0}} = \frac{0.5 \left(\frac{p}{p_{t_2}}\right) \sqrt{1 - \left(\frac{p}{p_{t_2}}\right)^{\frac{\gamma-1}{\gamma}}} r}{\left[\int_{0}^{s} \left(\frac{p}{p_{t_2}}\right)^{\frac{\omega\gamma-(1-w)}{\gamma}} \sqrt{1 - \left(\frac{p}{p_{t_2}}\right)^{\frac{\gamma-1}{\gamma}}} r^2 ds\right]^{1/2} \sqrt{\frac{1}{u_{\infty}} \left(\frac{du}{ds}\right)_{s=0,\alpha=0}} \left[\frac{\theta_{w}^{i}}{(\theta_{w}^{i})_{s=0}}\right]^{1/2}} (3)$$

where  $\theta_{W}$  is a function of the local velocity gradient. As noted in figure 9, equation (3) predicts higher maximum heating rates than equation (2). In general, the axisymmetric theory appears adequate for rapid estimates of heat transfer along the  $\phi = 0^{\circ}$  meridian.

More refined estimates of the heat-transfer distributions should result from a general solution to the three-dimensional boundary-layer equations. In order to investigate the effect of this, the general three-dimensional stagnation-point





theory of Reshotko (ref. 7) was applied at  $\alpha = 33^{\circ}$  for which case the velocity gradient along  $\phi' = 90^{\circ}$  direction was measured (see fig. 8). Reference 7 suggests that the axisymmetric stagnation-point heat transfer should be modified as follows:

$$\frac{h_{0,\alpha}}{h_{0,\alpha=0}} = \left[\frac{h_{0,\alpha}}{h_{0,\alpha=0}}\right]_{\text{axisym}} \left\{\frac{1 + \left(\frac{\text{dw}/\text{dz}}{\text{du}/\text{ds}}\right)_{\text{s=z=0}}}{2}\right\}^{1/2}$$
(4).

The agreement of measured and predicted  $h_0,\alpha/h_0,a=00$  is quite good (fig. 9(e)) and indicates that a generalized approach to the three-dimensional boundary-layer equations is desirable for refined calculations but is beyond the scope of the present report. However, better agreement between the predicted distribution and the data is obtained when equation (3) is multiplied by the braced term of equation (4). This is shown in figure 9(e) by the curve labeled equation (3), adjusted.

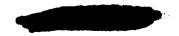
# Comparison of Air-Helium Data

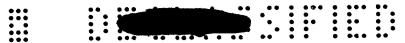
Before comparing helium and air data it is informative to study the theories used in predicting the ratios of  $p/p_{t_2}$  and  $h/h_{0,\alpha=00}$  with respect to their dependence upon  $\gamma$ . In order to illustrate the results of such a study only the data for  $\alpha=33^{\circ}$  are treated, but the results are applicable to the other angles of attack.

The theory of reference 3 predicted the pressure distribution in the vicinity of the stagnation point for angles of attack up to 25°, and Newtonian theory predicted the pressure distribution for S/R < 0. For  $M_{\infty} \gg 1$  Newtonian theory is unaffected by changes in  $\gamma$ . For increasing density ratio reference 3 predicts stagnation-point movement at a given angle of attack but results in almost identical pressure distributions when compared on the basis of distance from the predicted stagnation point. For example, at  $\alpha=25^{\circ}$  for a practical density ratio range (4  $\leq \rho_2/\rho_{\infty} \leq$  16), which for  $M_{\infty} \gg 1$  corresponds to  $1.667 \geq \gamma \geq 1.2$ , the predicted stagnation-point movement is from (S/R) $_{0}=0.74$  for  $\gamma=1.667$  to (S/R) $_{0}=0.81$  for  $\gamma=1.2$ . Since the movement of the stagnation point is small and the predicted distributions are practically identical, the pressure distribution should be insensitive to changes in  $\gamma$ . This conclusion can be tested by comparing data obtained in air and in helium at the same angle of attack.

Figure 10 presents the measured pressure ratio (p/p<sub>t2</sub>) plotted against S/R. The data were all obtained at  $\alpha \approx 33^{\circ}$  for a range of Mach numbers and  $\gamma$  as indicated. The effect of  $\gamma$  on the pressure distribution appears to be less than the experimental scatter.

Next, the effect of  $\gamma$  on equation (3) was studied and the results are shown in figure 11 where the distribution of heat-transfer coefficient (or cold-wall heating-rate distribution) is plotted against S/R. The pressure





distribution from figure 6(e) was used in this study. Again the effect of  $\gamma$ small, the greatest difference being found on the corner radius where maximum heating occurs. Also, the normalized stagnation-point velocity gradient, as presented in figure 8, can be shown to be independent of  $\gamma$  when identical pressure distributions are assumed as in the above study. It appears that the heattransfer distribution on the Apollo forebody is insensitive to  $\gamma$ . Since  $\gamma$  is a function of enthalpy, the implication of the foregoing is that the cold-wall heating-rate distribution is insensitive to enthalpy. This implication was also noted in reference 6. Thus the dimensionless distribution of heating rate is essentially constant, and the relative magnitudes of  $q_{\rm w}$  can be determined from the stagnation-point heating rate. Figure 12 presents measured ratios of  $h/h_{0.\alpha=0}$  obtained from various sources at  $\alpha \approx 33^{\circ}$  for the range of Mach numbers indicated. As expected the heat-transfer data compare well except on the corner radius where maximum heating occurs. It should be noted that this is a region which presents much experimental difficulty. The solid line represents the prediction of Kemp, Rose, and Detra for  $\gamma = 1.667$  adjusted by the factor in equation (4) as previously suggested.

#### CONCLUSIONS

- l. The external flow over the Apollo forebody changes from axisymmetric at  $\alpha = 0^{\circ}$  to nonaxisymmetric at  $\alpha = 33^{\circ}$ . However, the ratio of heat-transfer coefficients agreed reasonably well with the axisymmetric theory of reference 6 when measured surface pressures were used.
- 2. The movement of the stagnation point up to  $\alpha$  = 25° was adequately predicted by the theory of reference 3 and was less than that predicted by Newtonian theory.
- 3. At angle of attack the maximum heat transfer was measured on the corner radius and not at the stagnation point. Axisymmetric theory using measured pressure distribution predicted this.
- 4. A study of the theories for predicting pressure and heat-transfer distributions indicated that these quantities were not sensitive to changes in  $\gamma$ . A comparison of air and helium wind-tunnel data tended to substantiate this conclusion.

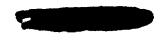
Ames Research Center
National Aeronautics and Space Administration
Moffett Field, Calif., July 17, 1963

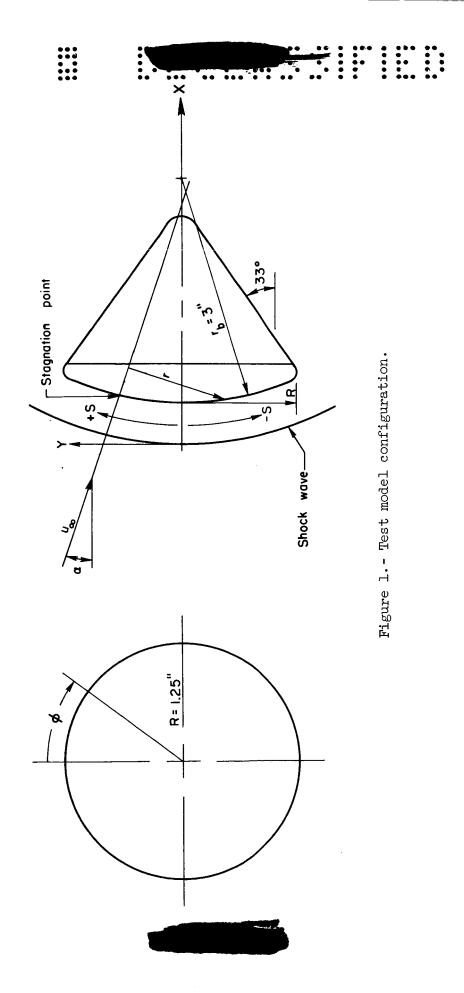
<sup>&</sup>lt;sup>1</sup>The data at  $M_{\infty}$  = 6.1, 7.5, and 9.1 were obtained from representatives of North American Aviation during a meeting at Ames Research Center. The  $M_{\infty}$  = 14.3 data were obtained by George Lee in the Ames are heated vertical 10-inch hypersonic wind tunnel.





- 1. Tendeland, Thorval, and Pearson, B. Douglas, Jr.: Effectiveness of Two Flap Controls on a Mercury Type Caspule at a Mach Number 15 in the Ames Hypersonic Helium Tunnel. NASA TM X-660, 1962.
- 2. Marvin, Joseph G.: Pressure and Heat-Transfer Distribution on the Afterbody of a Lifting Mercury-Type Capsule at Mach Number 15 in Helium. NASA TM X-783, 1963.
- 3. Kaattari, George E.: Predicted Gas Properties in the Shock Layer Ahead of Capsule-Type Vehicles at Angle of Attack. NASA TN D-1423, 1962.
- 4. Lees, Lester: Laminar Heat Transfer Over Blunt-Nosed Bodies at Hypersonic Flight Speeds. Jet Propulsion, vol. 26, no. 4, Apr. 1956, pp. 259-269, 274.
- 5. Wagner, Richard D., Jr., Pine, W. Clint, and Henderson, Arthur, Jr.:
  Laminar Heat-Transfer and Pressure-Distribution Studies on a Series of
  Reentry Nose Shapes at a Mach Number of 19.4 in Helium. NASA TN D-891,
  1961.
- 6. Kemp, Nelson H., Rose, Peter H., and Detra, Ralph W.: Laminar Heat Transfer Around Blunt Bodies in Dissociated Air. Jour. Aero/Space Sci., vol. 26, no. 7, July 1959, pp. 421-430.
- 7. Reshotko, Eli: Heat Transfer to a General Three-Dimensional Stagnation Point. Jet Propulsion, vol. 28, no. 1, Jan. 1958, pp. 58-60.
- 8. Gorowitz, H.: Data Report for NAA Shock Tunnel Tests (ST-4) of Apollo Command Module Models H-6 and PS-6. NASA Contract NAS 9-150, Rep. SID 62-1072, North American Aviation, Inc., August 1962.
- 9. Jones, Robert A.: Experimental Investigation of the Overall Pressure Distribution, Flow Field, and Afterbody Heat-Transfer Distribution of an Apollo Reentry Configuration at a Mach Number of 8. NASA TM X-813, 1963.
- 10. Hunt, D. N., and Smith, H. C.: Data Report for Apollo Model (PS-1) Wind Tunnel Test. NASA Contract NAS 9-150, Rep. SID 62-548, North American Aviation, Inc., May 1962.
- 11. Biss, W. J., and Emerson, D. X.: Experimental Heat Transfer Distributions Over Launch and Entry Configurations of an 0.045 Scale Apollo Model (H-2) at Mach Numbers of 8 and 10. Vol. 1-6, NASA Contract NAS 9-150, Rep. SID 62-993, North American Aviation, Inc., Sept. 1962.





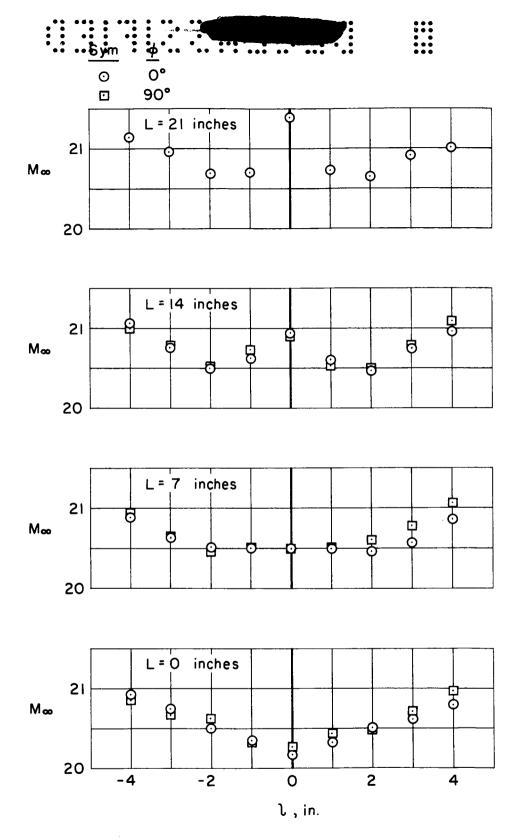


Figure 2.- Test-section Mach number survey at various locations along the tunnel center line for  $\,p_{\mbox{t}}$  = 2,000 psia.

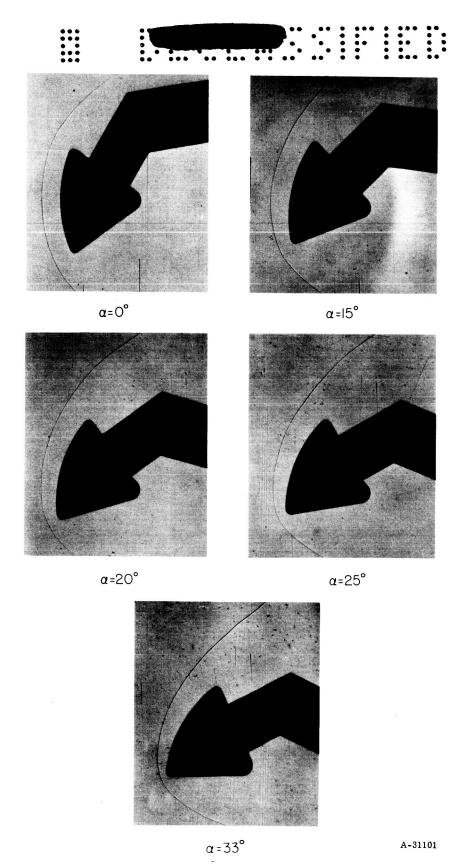


Figure 3.- Shadowgraphs of the shock-wave system for various angles of attack.

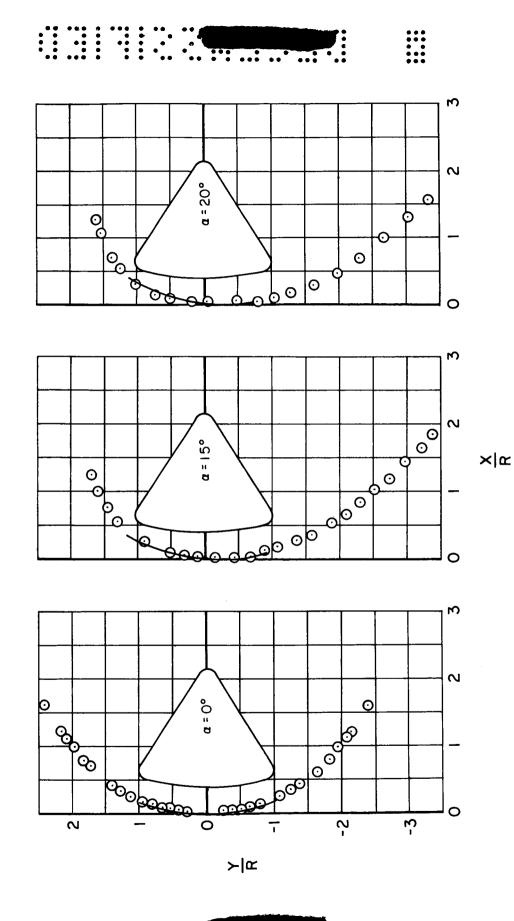


Figure 4. - Measured shock-wave shapes for various angles of attack.

(a)  $\alpha = 0^{\circ}$  to  $20^{\circ}$ 

Measured data from figure 3

0

Theory (reference 3)

0

0

0 0

<u>ે</u> એ

2

00

a = 33°

a =25°

0

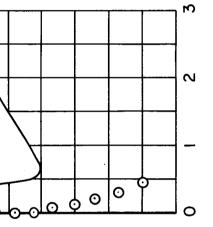
Measured data from figure 3

0

Theory (reference 3)

<u>o</u> 0 <u></u>0 2  $a = 37.5^{\circ}$ 0 <del>po</del> 0 0

×Iœ





3

2

0

5

6 O

0

-2

(b)  $\alpha = 25^{\circ} \text{ to } 37.5^{\circ}$ 

Figure 4. - Concluded.

>|œ

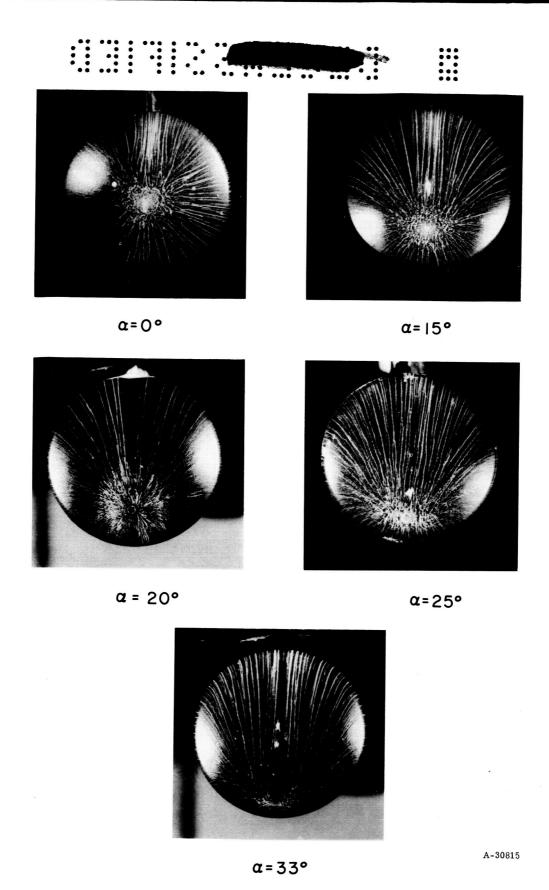


Figure 5.- Photographs of streamline patterns for various angles of attack.

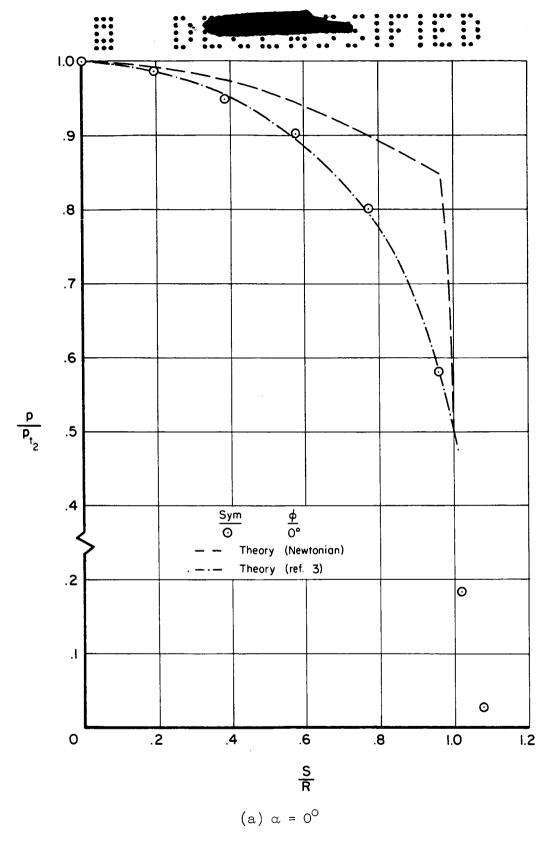
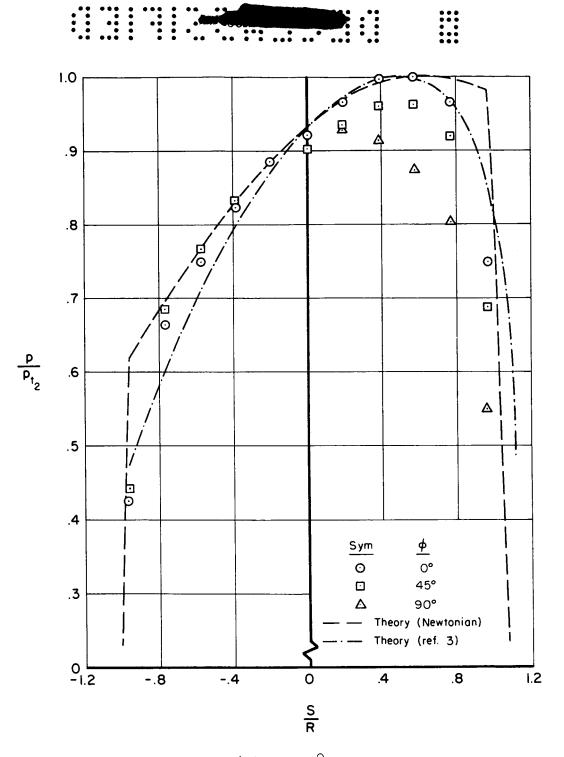
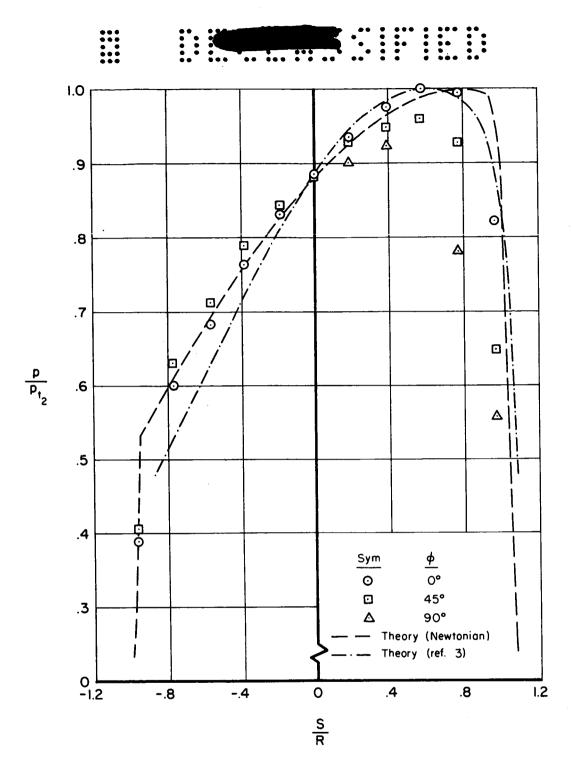


Figure 6.- Forebody surface pressures along various meridians for various angles of attack.



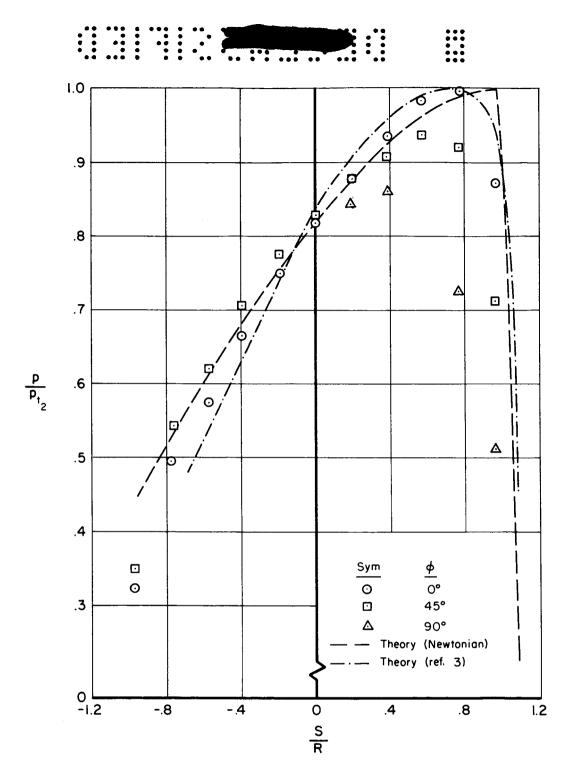
(b)  $\alpha = 15^{\circ}$ 

Figure 6.- Continued.



(c) 
$$\alpha = 20^{\circ}$$

Figure 6.- Continued.



(d) 
$$\alpha = 25^{\circ}$$

Figure 6. - Continued.



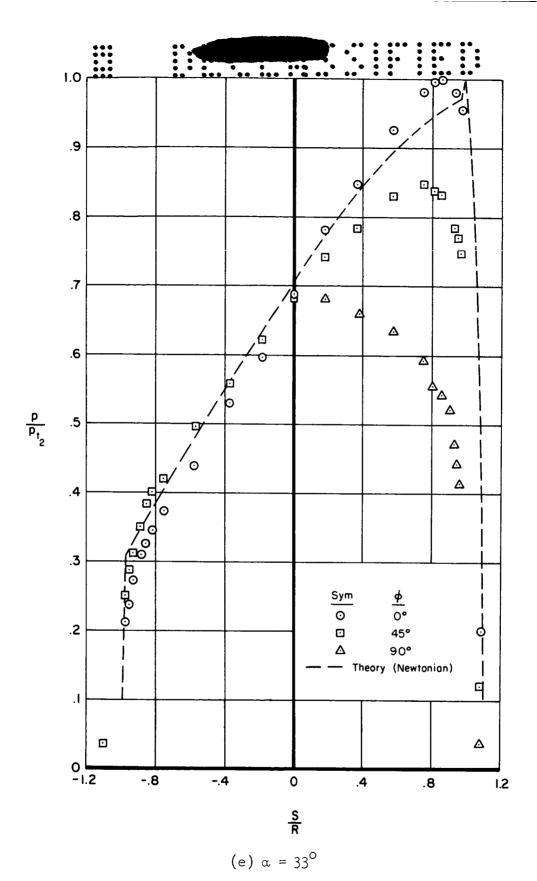


Figure 6.- Concluded.



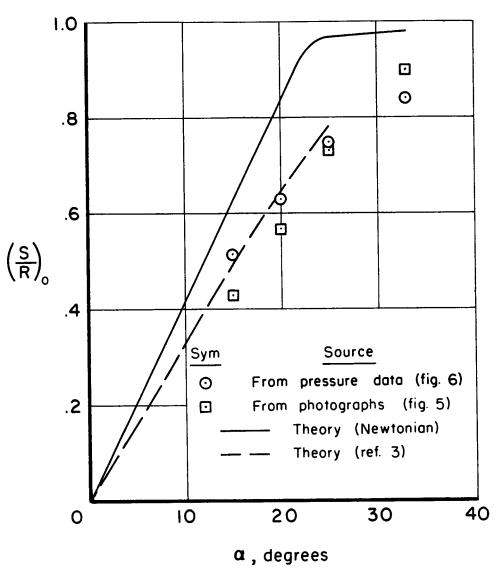


Figure 7.- Comparison of measured stagnation-point location with theory.

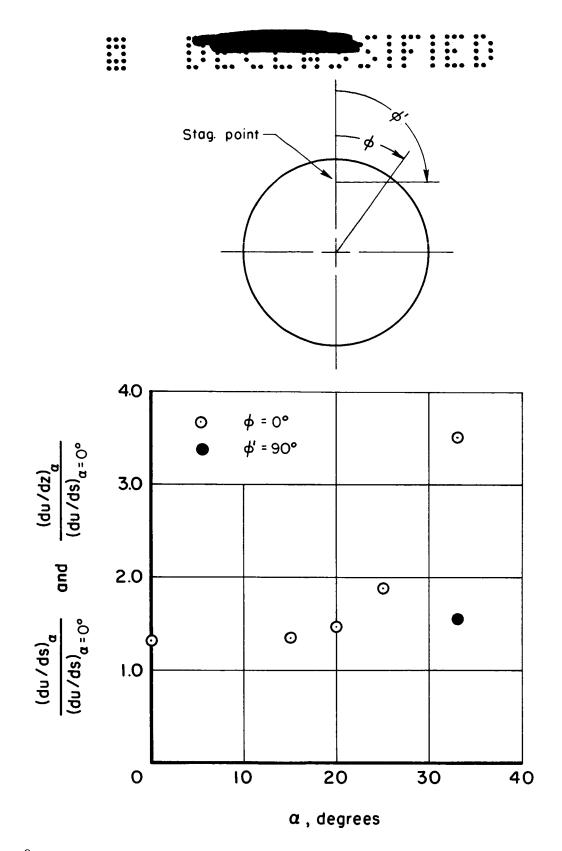


Figure 8.- Stagnation-point velocity gradient on the most windward meridian for various angles of attack normalized with respect to the velocity gradient predicted by Newtonian theroy for  $\alpha = 0^{\circ}$ .



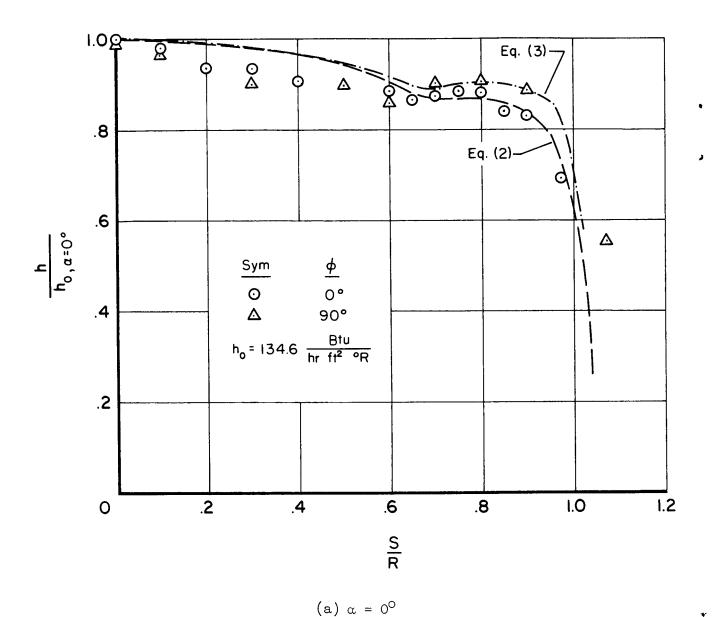
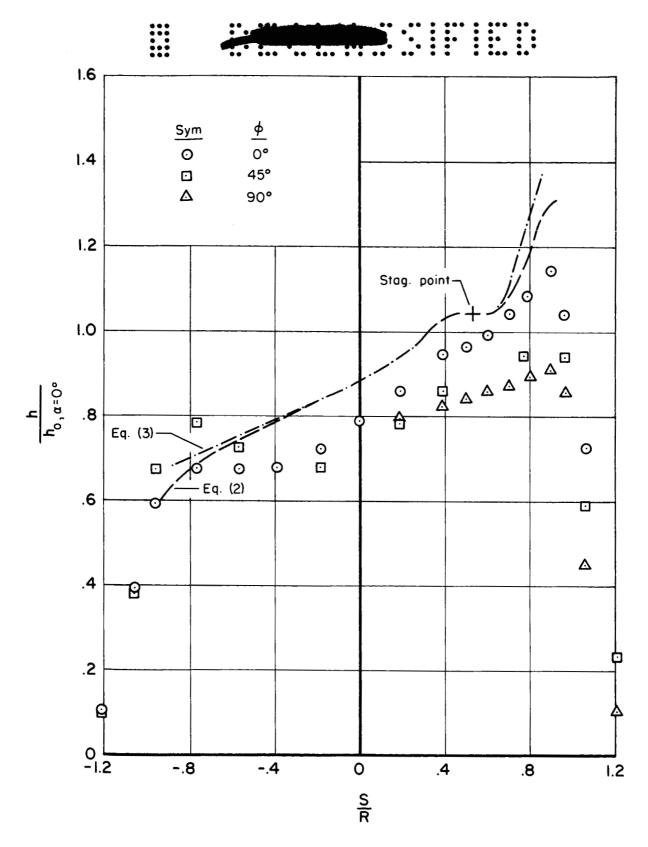


Figure 9.- Forebody heat-transfer coefficients along various meridians for various angles of attack.



(b)  $\alpha = 15^{\circ}$ 

Figure 9.- Continued.

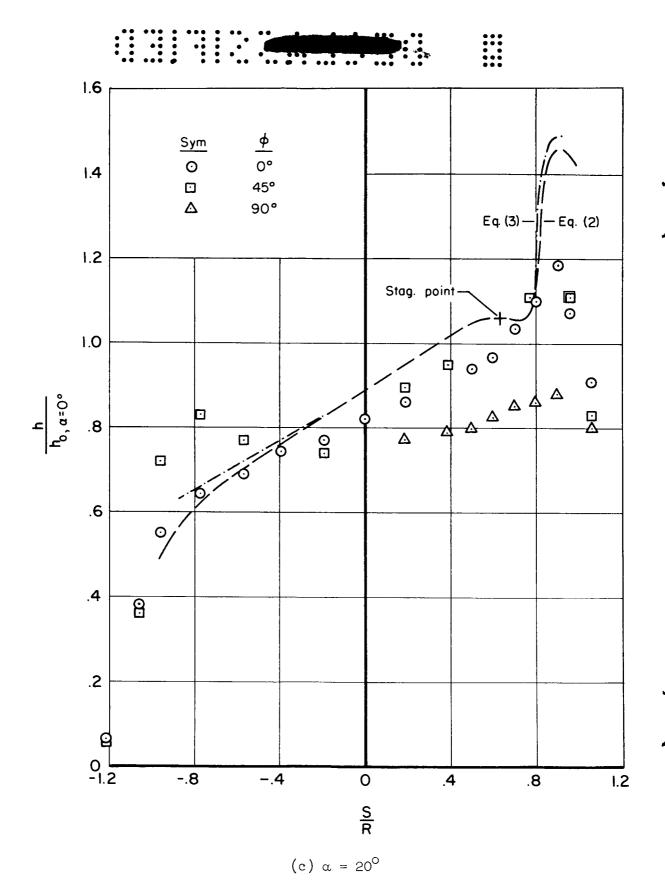


Figure 9. - Continued.

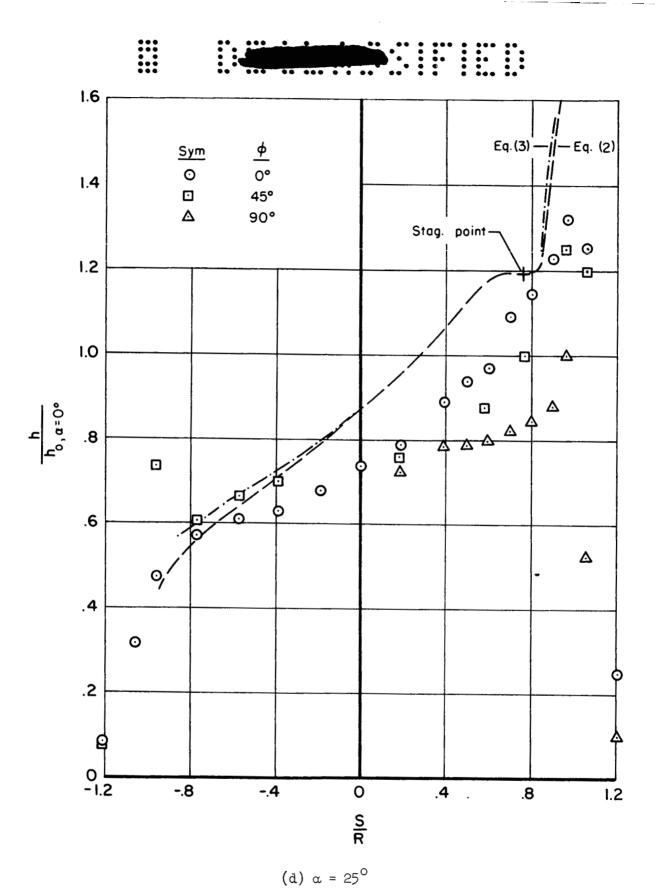
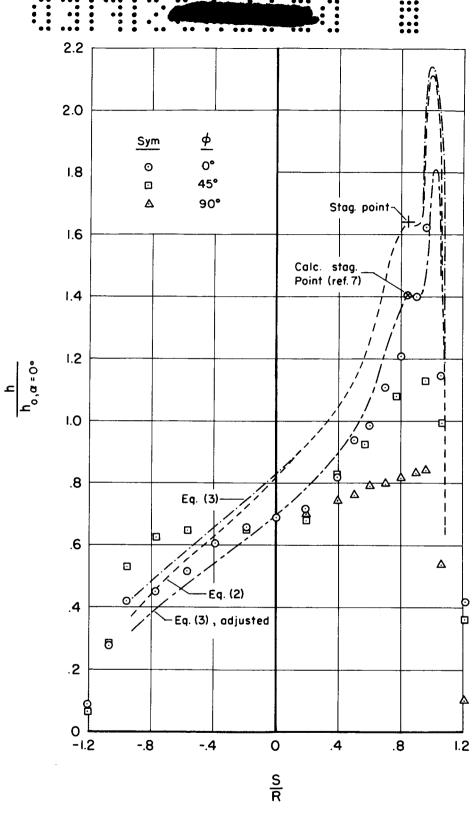


Figure 9. - Continued.



(e)  $\alpha = 33^{\circ}$ 

Figure 9. - Concluded.

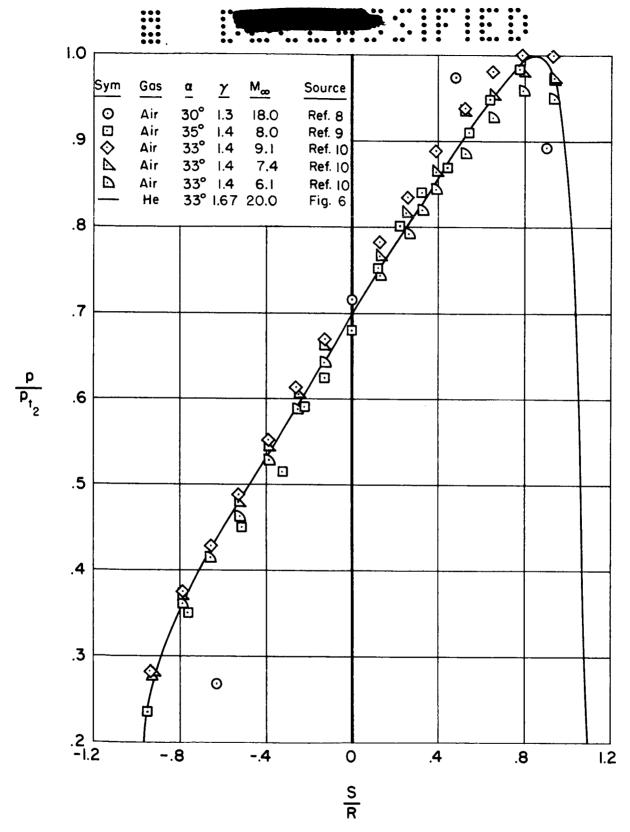


Figure 10.- Comparison of air and helium pressure distribution at  $~\alpha~\approx~33^{\circ}$  and  $\phi$  =  $0^{\circ}$  .



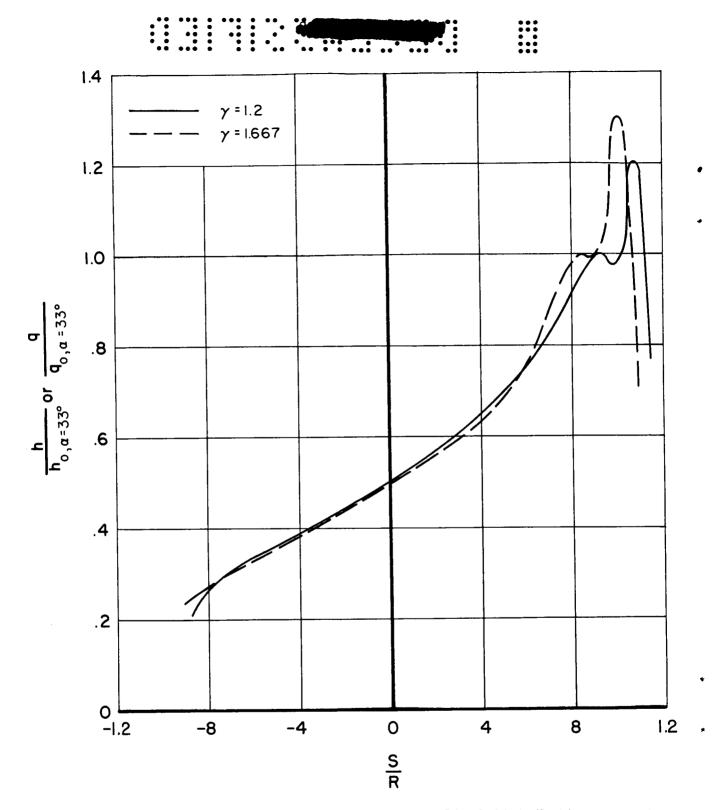


Figure 11.- Estimated effect of  $\gamma$  on the normalized distribution of heat transfer to the forebody at  $\alpha=33^{\circ}$  and  $\phi=0^{\circ}$ .

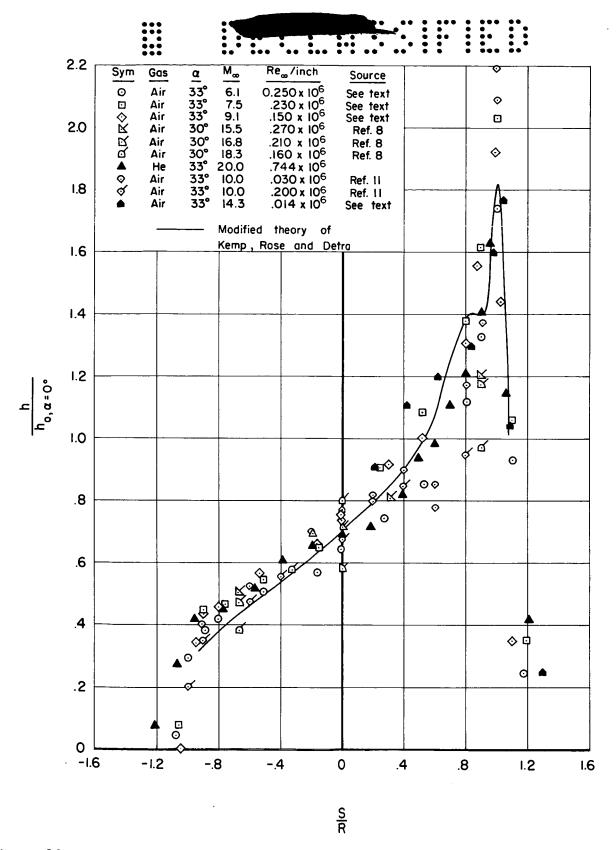


Figure 12.- Comparison of air and helium heat-transfer distribution at  $~\alpha=33^{\rm O}$  and  $~\phi=0^{\rm O}$  .